Effects of Martensite Content and Anisotropy on Hydrogen Fracture of Dual-Phase Steels

Boot, T.; Leivseth, E.; Fernández Iniesta, S.; Kömmelt, Pascal; Bottger, A.J.; Popovich, V.

DOI
10.3390/met15121333

Publication date
2025

Document Version
Final published version

Published in
Metals

metals

MDPI

Article

Effects of Martensite Content and Anisotropy on Hydrogen Fracture of Dual-Phase Steels

Tim Boot [1,*], Eirik Leivseth [1], Sara Fernández Iniesta [1], Pascal Kömmelt [2], Amarante J. Böttger [1] and Vera Popovich [1,*]

[1] Department of Materials Science & Engineering, Delft University of Technology (TU Delft), Mekelweg 2, 2628 CD Delft, The Netherlands
[2] Tata Steel, Research & Development, PO Box 10000, 1970 CA IJmuiden, The Netherlands
* Correspondence: t.boot@tudelft.nl (T.B.); v.popovich@tudelft.nl (V.P.)

Abstract

This work studies the hydrogen embrittlement (HE) behaviour of Dual-Phase steels with varying martensite content. Steels with martensite contents of 25 ± 5, 50 ± 4 and 78 ± 7% were realised by intercritically annealing an as-received DP steel. These steels were charged with hydrogen and consequently subjected to an in situ slow strain rate tensile test to characterise the embrittlement. It was found that the steel with 50% martensitic content showed the most ductility in air, but the highest embrittlement of 86 ± 10%. The extent of embrittlement does not increase further from the point that martensite forms a continuous network in the microstructure. The presence of martensite on the surface is linked to the formation of brittle crack initiation sites in these steels. Furthermore it was found that the anisotropic banded structure in the annealed steels promotes brittle crack propagation along the direction of banding, which originates from rolling process. This research shows that anisotropic martensite distributions as well as surface martensite should be avoided when developing rolled steels, to maximise HE resistance.

Keywords: hydrogen embrittlement; dual-phase steel; martensite; fractography; tensile testing

Academic Editor: Andrea Di Schino

Received: 24 October 2025
Revised: 21 November 2025
Accepted: 1 December 2025
Published: 3 December 2025

Citation: Boot, T.; Leivseth, E.; Iniesta, S.F.; Kömmelt, P.; Böttger, A.J.; Popovich, V. Effects of Martensite Content and Anisotropy on Hydrogen Fracture of Dual-Phase Steels. *Metals* **2025**, *15*, 1333. https://doi.org/10.3390/met15121333

1. Introduction

The automotive sector is a significant contributor to global CO_2 emissions since the majority of vehicles still use combustion engines, which burn fossil fuels [1]. Approximately 75% of the fuel consumption of modern cars is related to vehicle weight [2–4]. Reducing vehicle weight will therefore lead to CO_2 reductions. To allow a reduction in weight without compromising on passenger safety, the industry has been on the forefront of developing and using (Advanced) High-Strength Steels (AHSSs) in vehicles.

The most widely used types of Advanced High-Strength Steels (AHSSs) within the automotive sector are Dual-Phase (DP) steels [5]. DP steels combine the ductility of the ferritic phase with the strength of an interdispersed martensitic phase to obtain a low initial yield point, but a high strength with high initial strain hardening [6]. This results in good properties for formability and energy absorption [7]. DP steels make up around a third of the body-in-white of a modern car chassis [5], and are used in various components such as panels, pillars and shock reinforcement parts [8]. However, DP steels have been found to be susceptible to HE like other AHSSs [9–12]. Its susceptibility is related to the martensitic fraction, in which both the interphase boundary with ferrite and the grains

themselves can be hydrogen trap sites [13]. Decades of experience with DP steels have created a good understanding on how to alter the martensitic fraction and grain sizes, which has led to multiple studies characterising their effects on the HE of DP steels [14–19]. A comprehensive understanding, however, has still not completely been achieved [7,20,21].

Different literature sources suggest an HE behaviour that is divided into three regimes, based on martensite content [12,22]. When martensite comprises less than 10% of the microstructure, no HE is found, since the majority of the microstructure is ferritic and martensite islands are therefore spaced apart. The ferrite/martensite (F/M) interphase boundary is found to be the main hydrogen trap for this microstructure [12,23,24]. As the martensite content increases, martensite grains grow, the interphase area increases and more H is stored. When martensite grains grow large enough to connect to each other, a continuous martensite network is formed within the ferrite matrix. Wang et al. reason that at such martensite concentrations, 68.3% in their study, the F/M interphase area decreases and the hydrogen is stored inside the martensite instead [12]. HE is found to no longer increase at higher martensite fractions from this point by Davies [22], although Wang et al. find that it does increase as the amount of absorbed hydrogen still increases and the diffusivity of hydrogen decreases [12].

Fracture in DP steels charged with hydrogen is found to initiate either on the F/M interphase, or within martensite grains. DP grades with a high ferrite fraction can accommodate more strain, but develop significant strain partitioning at the interphase boundary between the soft ferrite and the hard martensite [12,25]. A locally high plastic strain increases the capacity for hydrogen absorption [24,26,27], finally leading to decohesion of the interphase. Ferrite between martensite islands acts as a crack propagation barrier, but it decreases in effectiveness in microstructures with larger martensite grains, because the ferrite in between them decreases in thickness [12]. Moreover, the ferrite reduces in capacity to act as a barrier when hydrogen is introduced into the microstructure, as shown by Koyama et al. [28]. Higher martensite fractions give the DP steel a higher strength, but sacrifice in strain since the martensitic network supports the applied stress and does not allow the ferrite to deform. Furthermore, cracks can propagate purely through the martensite at this point, and the crack growth inhibiting role of the ferrite disappears. The exact point at which this happens, though, seems to vary between microstructures. Davies reports it to be around 30% martensite [22], whereas Wang et al. report it to be 68.3% [12].

The effects of microstructural morphology were reported by Rodoni et al., who observed crack initiation on the F/M interphase [29]. Cracks propagated through bands of martensite within a DP matrix, perpendicular to the rolling direction. The cracks were arrested upon meeting a ferrite grain. This anisotropy is often found in rolled sheets, and could provide better HE resistance in a particular direction. Sun et al, for example, engineered a microscale lamellar structure of ferrite and martensite grains perpendicular to the tensile direction, which improved HE resistance compared to an untreated material [30]. Microstructural anisotropy should therefore be considered when investigating fracture behaviour of a DP steel.

There are two points of ongoing discussion in the literature that require further research. Firstly, opposing views have been published on whether HE in DP steels increases past the point of formation of a connected martensitic matrix. This means that the effects of anisotropy should be considered, since rolling-induced deformation influences the formation of martensite bands in the rolling direction. This work addresses these issues by discussing results regarding DP steels in a cold-rolled sheet, elucidating the role of the anisotropic martensite configuration in hydrogen embrittlement, as well as fracture initiation and propagation within the microstructure.

2. Material and Methods

The as-received DP steel studied in this work is a 1 mm thick commercial grade DP1000 steel supplied by TATA Steel in IJmuiden, of which the composition is shown in Table 1. The microstructure, shown in Figure 1, is made up of a connected network of martensite with refined 1.7 ± 0.7 µm ferrite grains in between. The martensite content in the as-received alloy is approximately 68% as determined by using the ImageJ analysis software version 1.54g on Figure 1. Heat treatment experiments were performed to vary the martensitic content of the DP steel in order to study the effect of martensite fraction and structure on the HE behaviour.

Table 1. Alloy content of the as-received DP steel used in this research in wt%.

Fe (Balance)	C	Mn	Cr	Si	Al
97.03	0.14	2.15	0.54	0.13	0.02

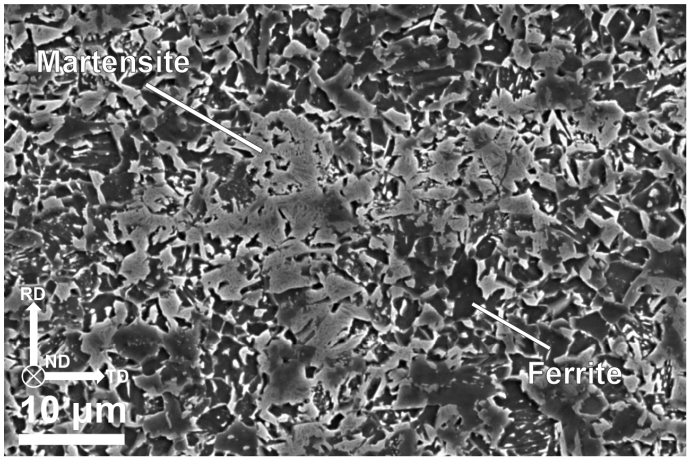

Figure 1. The as-received DP1000 microstructure. Martensite is shown as the lighter phase, and ferrite as the darker.

2.1. Heat Treatments and Characterisation

The focus of the work discussed in this study is to tailor DP steels with different martensite fractions in order to assess their HE susceptibility. Heat treatments were performed in a Gleeble 3800-GTC thermomechanical simulator (Dynamic Systems Inc., Poestenkill, NY, USA), which consisted of a heating step to 900 °C at 10 °C/s per second, holding there for 3 min, cooling down to three different intercritical annealing temperatures at 1 °C/s, holding for 10 min and finally air quenching to room temperature. Intercritical annealing temperatures of 590, 610, 630, 650 and 670 °C were chosen for trial heat treatments on a Bähr FIL805A/D quenching (TA Instruments, New Castle, DE, USA) and deformation dilatometer, based on the Ac_1 and Ac_3 temperatures that were determined as 686 °C and 571 °C. Three final heat treatments temperatures of 590, 630 and 670 °C were then chosen for Gleeble simulation.

The martensite fraction was determined through both optical (OM) and electron microscopy (SEM), as well as electron backscattering diffraction (EBSD). For all these techniques, samples were embedded in thermoset resin, sanded and polished to a 1 µm finish, and finally etched in a 5% nital solution for 8 s. Instead of etching, EBSD specimens were further polished to a 0.04 µm colloidal silica OPS finish. Optical microscopy images were taken on a Keyence VHX-7000 digital microscope (Keyence International, Mechelen, Belgium), which includes automated measurement of area fractions based on brightness. Electron Microscopy images were taken on a JEOL JST-IT100 dekstop SEM (JEOL Europe,

Nieuw-Vennep, The Netherlands). In this case, images were exported and analysed externally using ImageJ software. EBSD was performed inside a Thermo-Fisher Helios G4 PFIB UXe HRSEM (Thermo Fisher Scientific, Eindhoven, The Netherlands) equipped with an EDAX Technology APED camera. Measurements were performed at an acceleration voltage of 15 kV, with a probe current of 6.4 nA and a step size of 100 nm. The ferritic and martensitic phases were distinguished by colour in OM, by brightness in SEM and by image quality in EBSD. Examples of the images used to determine the martensite fraction and ferrite/martensite interphase density are shown in Supplementary Figure S1. Three different areas were measured for each heat treatment condition for all techniques. Martensite fractions were found to correspond well between techniques, and the average of the techniques will be used throughout this work. All fractographic images throughout this study were also obtained on the JEOL JST-IT100 desktop SEM. Vickers Hardness measurements with a force of 1 kg were performed on a Struers Durascan automatic hardness tester.

2.2. Hydrogen Charging and Mechanical Testing

Specimens heat-treated in the Gleeble were electron discharge machined (EDM) to a double neck-geometry that is depicted in Figure 2, where TD is both the transverse rolling direction and the tensile direction. Double necking is necessary because the edges of a single-necked specimen are not heat-treated homogeneously in the Gleeble, and would have a different microstructure from the centreline. Moreover, it localises fracture to the zone that was treated in the Gleeble and has the desired microstructure. The specimens were subjected to slow strain rate tensile (SSRT) tests in a ZwickRoell Z100 universal tensile tester (ZwickRoell, Venlo, The Netherlands) fitted with the same in situ electrochemical hydrogen charging setup that is discussed in our previous work, after being sanded up to a P1200 finish on all surfaces [31,32]. The bath is filled with a solution of 3.5% NaCl + 3 g/L ammonium thiocyanate (NH_4SCN), which is used to charge the specimen at a current density of 1 mA/cm^2. Each specimen is pre-charged for 2 h before being strained until fracture at a strain rate of $3.125 \cdot 10^{-5}$/s. The strain is recorded using an Epsilon 4030 submersible extensometer (Epsilon Technology Corp., Jackson, WY, USA). The extent of HE in the specimens was characterised as the Hydrogen Embrittlement Index (*HEI*), which is calculated according to Equation (1), where ϵ_f^{Air} is the fracture strain in air, and $\epsilon_f^{H_2}$ is that in hydrogen.

$$HEI[\%] = \frac{\epsilon_f^{Air} - \epsilon_f^{H_2}}{\epsilon_f^{Air}} * 100\% \quad (1)$$

Benchmark tests to obtain the mechanical properties of the DP steels without hydrogen were performed ex situ on specimens containing a single gauge section similar to the outer dimensions of the sample shown in Figure 2. This was done to obtain more accurate data for the whole stress–strain curve of the non-hydrogenated specimens on a longer specimen gauge.

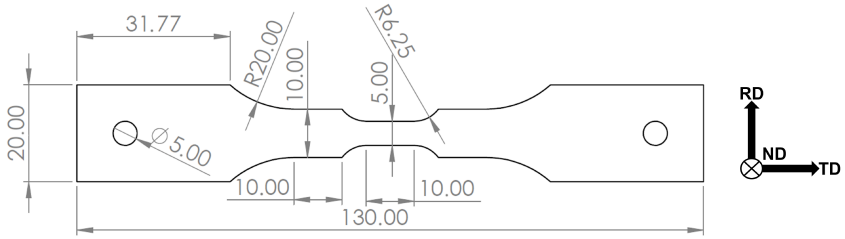

Figure 2. Sample geometry after Gleeble testing. The axis system is relative to the rolling direction (RD), transverse direction (TD) and normal direction (ND) of the rolled sheet. All dimensions are in mm.

Section 3.4 discusses a specimen from a separate study, the DP1000 steel with identical composition, which shows similar fracture behaviour to the treated DP steels in this work [33]. This specimen was charged with hydrogen in a bath of 0.5 M H_2SO_4 + 5 g/L thiourea for 15 min at a current density of 0.84 mA/cm^2 before being electroplated with Zn to inhibit hydrogen effusion. It was then subjected to a constant tensile load of 40% of its fracture load. The specimen geometry, including a notch introduced to localise the area of fracture, is show in Figure 3.

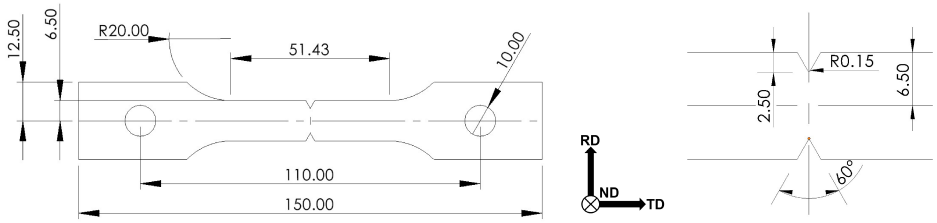

Figure 3. Geometry of the notched DP1000 specimen. The axis system is relative to the rolling direction (RD), transverse direction (TD) and normal direction (ND) of the rolled sheet. All dimensions are in mm.

Hydrogen contents were measured on a Bruker Galileo G8 with added IR07 infrared furnace (Benelux Scientific, Ede, the Netherlands). Specimens taken from the second neck of the in situ tested samples were measured in the impulse furnace of the G8. This is a melt extraction measurement performed at approximately 1700 °C where all hydrogen trapped in the specimen is released, measured over time and integrated into the total hydrogen content. This means that there is no distinction between diffusible and trapped hydrogen in the latter measurements, but since the amount of trapped hydrogen in DP steels has been shown to be negligible, they can be both qualitatively and quantitatively compared [34].

3. Results and Discussion

3.1. Creation of Microstructures

Initial heat treatments to vary the martensite content in the DP steel were conducted in the dilatometer. The martensite content was measured through OM, SEM and EBSD methods, and the results are shown in Figure 4. It is immediately visible that there is an increasing trend in martensite content with increasing annealing temperature from a minimum of 25% at 590 °C to a maximum of 78% at 670 °C. The average martensite content calculated from each technique are given in Table 2. In order to limit control parameters while retaining sufficiently distinct martensite contents, the heat treatments at 590, 630 and 670 °C were repeated on tensile samples in the Gleeble. Overviews of the resulting microstructures obtained from SEM are displayed in Figure 5. The martensite islands in the 590 °C specimen exist within a connected network of ferritic grains. This changes in the 630 °C specimen where all martensite grains are in contact with each other, although ferrite grains do still contact each other as well. The complete isolation of ferrite into separate islands is observed in the 670 °C specimen where martensite forms most of the microstructure. Connected martensite network formation thus forms at around 50% martensite, which is higher than the 30% that Davies reported [22], but lower than the 68% that Wang et al. found [12]. Since this is where both authors found hydrogen embrittlement to reach a maximum, it can be expected to level off after 50% in this research.

Other than the martensite content, the line density per area of the ferrite/martensite interphase (in µm/µm^{-2} or µm^{-1}) could also be calculated from micrographs. It can be seen from Table 2 that the interphase density keeps increasing even at a martensite content of 78%, which directly opposes findings in the literature [12]. The unexpected increase in

F/M interphase is a result of the change in size and shape of ferritic grains as the annealing temperature increases. Figure 5c shows that the ferrite grains that exist in between the martensite matrix have a very small size and an elongated shape, which can both contribute to a high interphase density for a relatively low ferrite content.

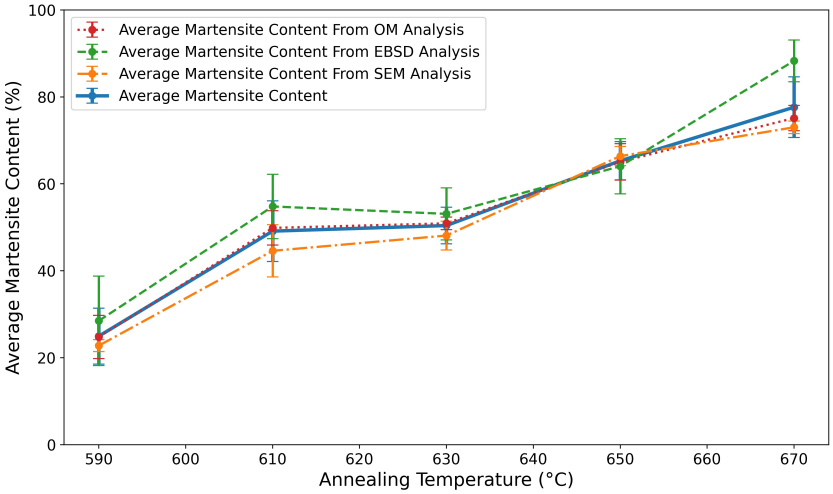

Figure 4. Martensite content after intercritical heat treatments. Three separate methods, namely optical microscopy (OM), scanning electron microscopy (SEM) and electron backscatter diffraction (EBSD), were used to separately calculate the martensite content.

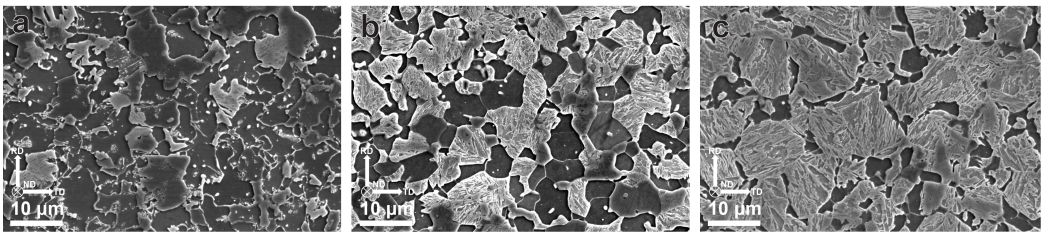

Figure 5. Microstructural overviews of tensile specimens annealed at (**a**) 590 °C, (**b**) 630 °C and (**c**) 670 °C during the Gleeble treatment. Martensite is shown as the lighter phase, and ferrite as the darker.

Table 2. Hardness, martensite content, martensite grain size, ferrite/martensite interphase density and hydrogen content for the investigated microstructures.

Annealing Temp. [°C]	Hardness [HV1]	Martensite Content [%]	Ms Grain Size [µm]	F/M Interphase Density [µm /µm^2·10^{-2}]	H Content [wppm]
590	238 ± 25	25 ± 5	3.9 ± 2.6	2.65 ± 0.61	1.16 ± 0.11
630	286 ± 13	50 ± 4	5.9 ± 3.2	3.12 ± 0.57	1.29 ± 0.13
670	344 ± 12	78 ± 7	7.4 ± 3.4	3.83 ± 0.44	1.58 ± 0.27

3.2. Hydrogen Trapping

The total hydrogen concentrations are listed in Table 2 together with the other microstructural characteristics. They are visually represented in Figure 6, which shows that all three measures increase with increasing annealing temperature. In the literature, the F/M interphase is often proposed as the main microstructural feature responsible for hydrogen trapping in DP steels [10,12,23,24]. These studies, however, consider the F/M interphase to decrease in density at high martensite contents. Wang et al. propose a shift in hydrogen trapping from the interphase towards the interior of the martensite grains [12]. As can be observed in Figure 6, however, the F/M interphase density keeps increasing at high

martensite contents in this study. This is likely caused by the refinement of the ferrite grains, which causes an increase in aspect ratio, which can be seen in Figure 5c. This results in an increase in F/M interphase area relative to their size. The increasing trend also matches that of the hydrogen content more closely than the increase in martensite content. This suggests that the F/M interphase remains the main contributor to hydrogen trapping even at a martensite content of 78%. In reality, however, the martensite will always trap some hydrogen, so the increased absorption will be due to both factors. In order to distinguish between their relative contributions, TDS measurements should be performed on a larger sample mass for higher accuracy to be able to distinguish between hydrogen desorbed from these separate traps.

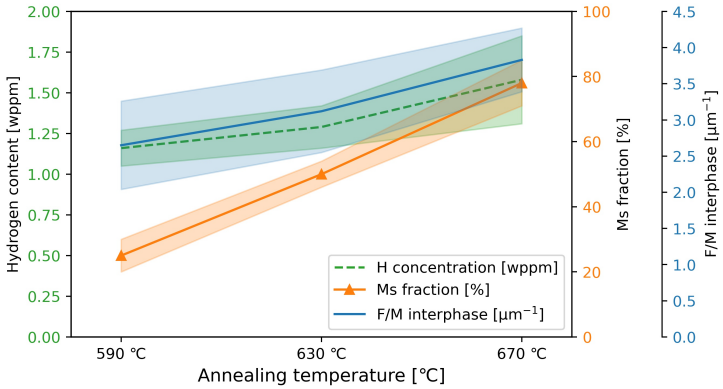

Figure 6. The total hydrogen concentration in wppm, martensite content in % and ferrite/martensite interphase density in μm^{-1} for the steels annealed at all three temperatures.

3.3. Mechanical Behaviour

Curves of the slow strain rate tensile (SSRT) tests for all three specimen sets are shown in Figure 7, and an overview of all data is shown in Table 3. As the martensite content increases, it has more capacity to accommodate the stress, and the strength of the steels increases. The 630 °C steel in particular shows beneficial properties of a relatively high strength and a considerable fracture strain of up to 12.6 ± 0.6%, as a result of its favourable ratio between ferrite and martensite. Unexpectedly, both strength and ductility for this steel are higher than that for the 590 °C steel, which fractures at 8.4 ± 1.7%. The 670 °C has similar strain to the 590 °C steel, but a higher strength of 1115 ± 15 MPa. As is characteristic of DP steels, plastic deformation in the ferritic phase starts early on in the tensile curve, which creates a gradual yield point and significant strain hardening.

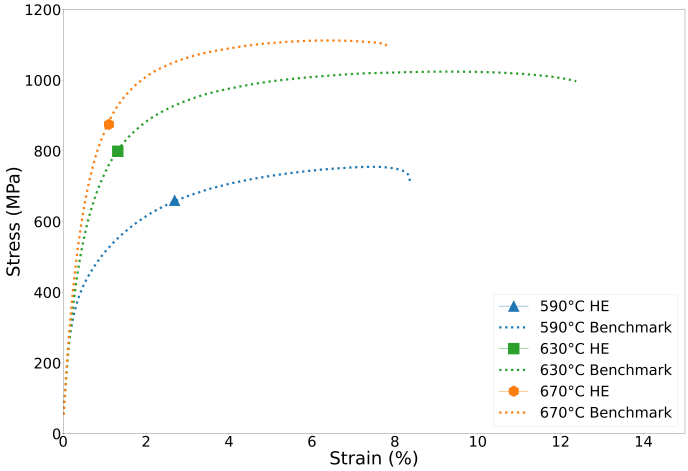

Figure 7. Slow strain rate tensile (SSRT) benchmark curves of the three steels tested in air, as well as the points of fracture when tested in hydrogen.

Table 3. Ultimate tensile strength (UTS) and fracture strains for all the investigated microstructures in air and charged with hydrogen, as well as the Hydrogen Embrittlement Index (HEI).

Annealing Temperature [°C]	UTS [MPa]	Fracture Strain [%]	UTS in H [MPa]	Fract. Strain in H [%]	HEI [%]
590	756 ± 20	8.4 ± 1.7	677 ± 21	4.1 ± 0.7	51 ± 39
630	1025 ± 8	12.6 ± 0.6	798 ± 35	1.8 ± 0.2	86 ± 10
670	1115 ± 15	8.2 ± 0.8	877 ± 20	1.6 ± 0.1	80 ± 19

Behaviour in a hydrogen environment differs significantly from that in air for all tested steels. Fracture occurs during strain hardening, which results in a reduction of both strength and ductility. The 590 °C steel retains the most of its ductility compared to the other steels, with a fracture strain of 4.1 ± 0.7% which corresponds to an HEI of 51 ± 39%. The ferritic phase can accommodate more strain in a hydrogen environment than the martensitic phase. Since the ferrite still forms a connected network in the 590 °C steel, this is the reason for its lesser degree of embrittlement compared to the other steels, although it still loses half its total ductility. An interesting finding in these curves is that the fracture strain of the 630 °C and 670 °C steels are very similar at 1.8 ± 0.2 % and 1.6 ± 0.1%, respectively. The HEI factors of these steels are relatively similar at 86 ± 10% and 80 ± 19%. While the steels therefore seem to perform comparably, it means that the 630 °C loses the higher ductility that made it perform better in the benchmark tests. The HEI stabilises from a certain martensite content, in this case 50%, which has been explain as a result of the fact that the martensite forms a connected network that allows for easy crack propagation [12,22]. Fracture initiation presumably happens at a similar plastic deformation for the 630 °C and 670 °C steels, and since both have martensitic networks, any difference in ferrite content or distribution becomes unimportant for the final fracture. Since the 670 °C retains a higher strength at a similar fracture strain, it performs better in the mechanical test than the 630 °C steel, although its performance is significantly reduced compared to a case without hydrogen.

Even though the only steel that shows some plastic strain in the tensile curves after hydrogen charging seems to be the the 590 °C annealed steel, it can be observed in the other specimens as well. The plastic deformation becomes visible in Kernel Average Misorientation (KAM) maps obtained 150 µm below the fracture surface of the 630 °C and 670 °C annealed specimens, as shown in Figure 8. Figure 8a shows a specimen annealed at 630 °C where it can be observed that localised areas of deformation are present around martensitic grains within the ferrite matrix, whereas larger ferrite grains remain relatively undeformed. In the 670 °C annealed specimen shown in Figure 8b, the deformation is strongly present on the interphase boundary between the martensite and interdispersed ferrite grains, whereas it is lower in the grain interior. The localisation of plastic strain, and therefore dislocations, on and around the F/M interphase has two effects. Firstly, it masks the appearance of global plastic strain in the tensile curve, which suggests that the extent of plastic deformation in the specimens is smaller than it actually is based on microstructural observations. Secondly, dislocations generated during deformation cause a significantly increased hydrogen absorption, as discussed in detail in our previous work on the effect of plastic deformation on HE fracture of ferritic HSLA steel [32]. This means that hydrogen concentrations will also be localised to the F/M interphase boundary, which could cause accelerated fracture initiation on the interphase and propagation through the martensite grain.

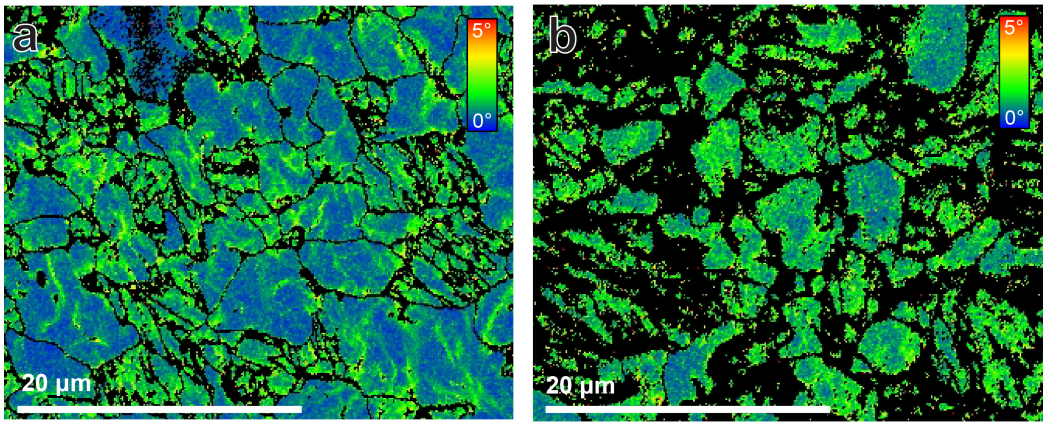

Figure 8. Kernel Average Misorientation (KAM) maps made 150 µm beneath the fracture surface of specimens annealed at (**a**) 630 °C and (**b**) 670 °C. Black areas signify non-indexed areas, which correspond to either grain boundaries or martensitic regions within the microstructure.

3.4. The Role of Martensite in Fracture Initiation

The presence of martensite in the microstructure of DP steels has a definite influence on its fracture behaviour, especially in a hydrogen environment. The influence on crack initiation is illustrated by studying an as-received DP1000 specimen that was subjected to a constant load after being charged to a hydrogen content of 1.7 wppm [33], which is similar to the specimens in this work. Figure 9 shows fractographic and cross-section SEM images of this specimen. A laser-cut notch in the specimen introduced to localise fracture is observed at higher magnification in Figure 9b. The figure clearly shows the existence of a surface region that is fully martensitic around the notch. This is a direct result of the laser cutting that was used to machine the notch, which causes local heating and cooling fast enough for martensite to form. Figure 9c shows a cross-section of the fracture surface shown in Figure 9a that visualises the brittle fracture through the martensitic region. The fracture surface is flat, which is characteristic of brittle QC fracture [35,36] , until it reaches the DP microstructure beyond the martensitic band. After this point, it deviates upward and the microstructure exhibits more deformation, which can be observed by the deformed grains on the right. The length of the flat brittle crack surface moreover corresponds to the width of the brittle zone of approximately 100 µm in width on the fracture surface in Figure 9a, which corresponds to hydrogen induced QC fracture. This fracture behaviour is a likely result of the surface martensite that is saturated with hydrogen upon charging, and which leads to brittle fracture initiation at these sites.

The same reasoning can be applied to the intercritically annealed samples with varying martensitic content tested in in situ SSRT. Cross-sectional electron micrographs of the short and long sides of a 590 °C annealed specimen are shown in Figure 10. Figure 10a shows the microstructure beneath the surface of the double neck that was cut using EDM. This method of sample cutting is preferred in hydrogen embrittlement research since it does not induce any deformation nor heat onto the resulting surface except for an oxide layer that can be polished off easily. This means that unlike laser-cutting, EDM does not induce martensitic surface structures. It does mean that EDM can expose existing martensite by cutting through martensite grains that are pre-existing in the specimens, as can be seen in Figure 10a. This is in contrast to the surfaces that were present from the rolling process, and were not EMD machined, which do not show any presence of martensite in Figure 10b. The fact that martensite is not present here is likely a result of carbon effusion from the near-surface regions during the intercritical annealing, which inhibited any martensite formation during quenching. Taking into account the presence of martensite on the side

surface, it follows that cracks preferentially initiated here since the surface martensite would be saturated with hydrogen during pre-charging of the specimens.

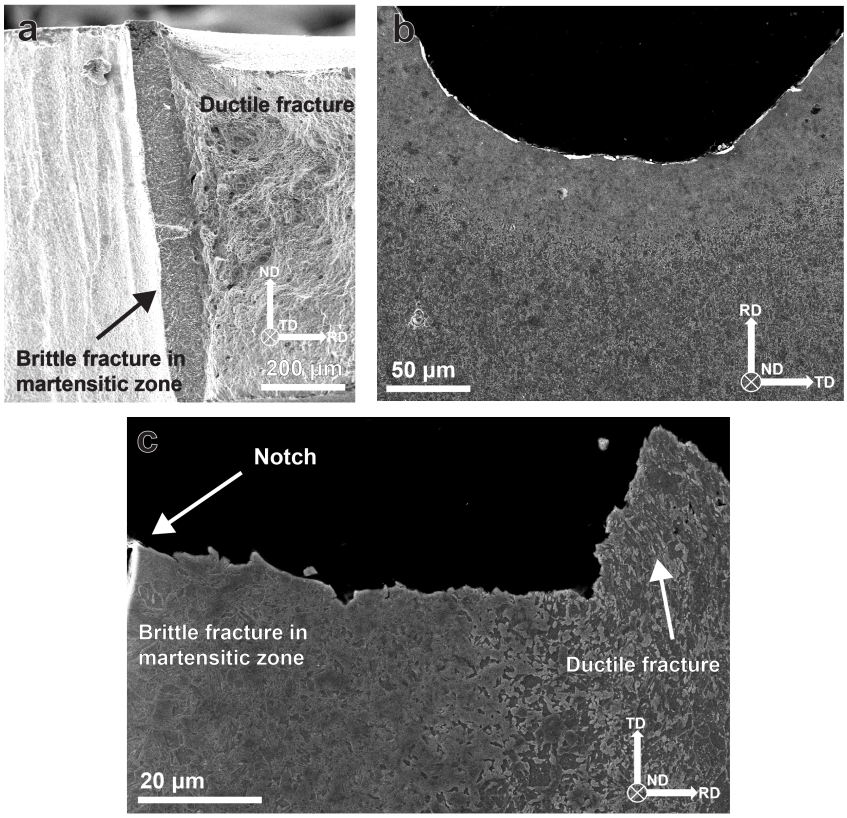

Figure 9. Cross-sections of the as-received DP steel subjected to constant load until fracture. (**b**) A martensitic structure around the notch surface, which corresponds to the brittle fracture zone on (**a**) the fracture surface and (**c**) the fracture cross-section.

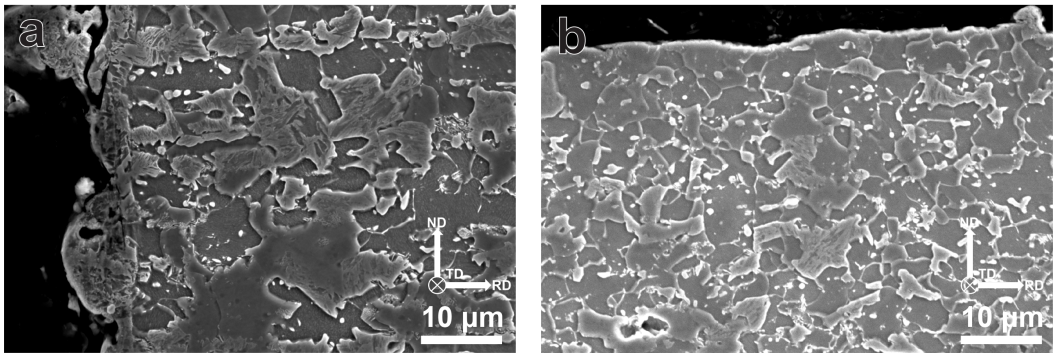

Figure 10. Cross-sections of the microstructure around the surface of a 590 °C specimen. (**a**) The short side edges of the specimen that was machined with EMD and (**b**) the surfaces created after rolling.

3.5. The Role of Martensite in Fracture Propagation

In order to study the role of martensite on the fracture propagation behaviour of these steels, the fracture surfaces were observed for traces of brittle fracture in the martensitic phase. They are shown in Figure 11, which includes higher magnification insets of brittle and ductile fracture zones specifically. A first observation to be made is that there is a distinct fracture band present in the 590 °C steel in Figure 11a, which corresponds to a sample-wide zone of brittle fracture relating to the Quasi-Cleavage (QC) fracture mode. Around the band, the fracture surface shows dimples. Similar bands seem to arise in the 630 °C specimens (Figure 11b), but the higher magnification insets show a brittle fracture

surface only around the short edge of the specimen, whereas the middle exhibits mixed-mode fracture between dimples and brittle facets. The 670 °C specimen in Figure 11c conversely shows a wider band, but brittle fracture is once again only found near the short edge. The fact that brittle fracture emerges on the short side of all specimens indicates that the crack likely initiated here and propagated towards the middle along the rolling plane of the steel sheet. It is counter-intuitive, however, that the specimen showing a QC fracture surface most explicitly is the one with the lowest HEI.

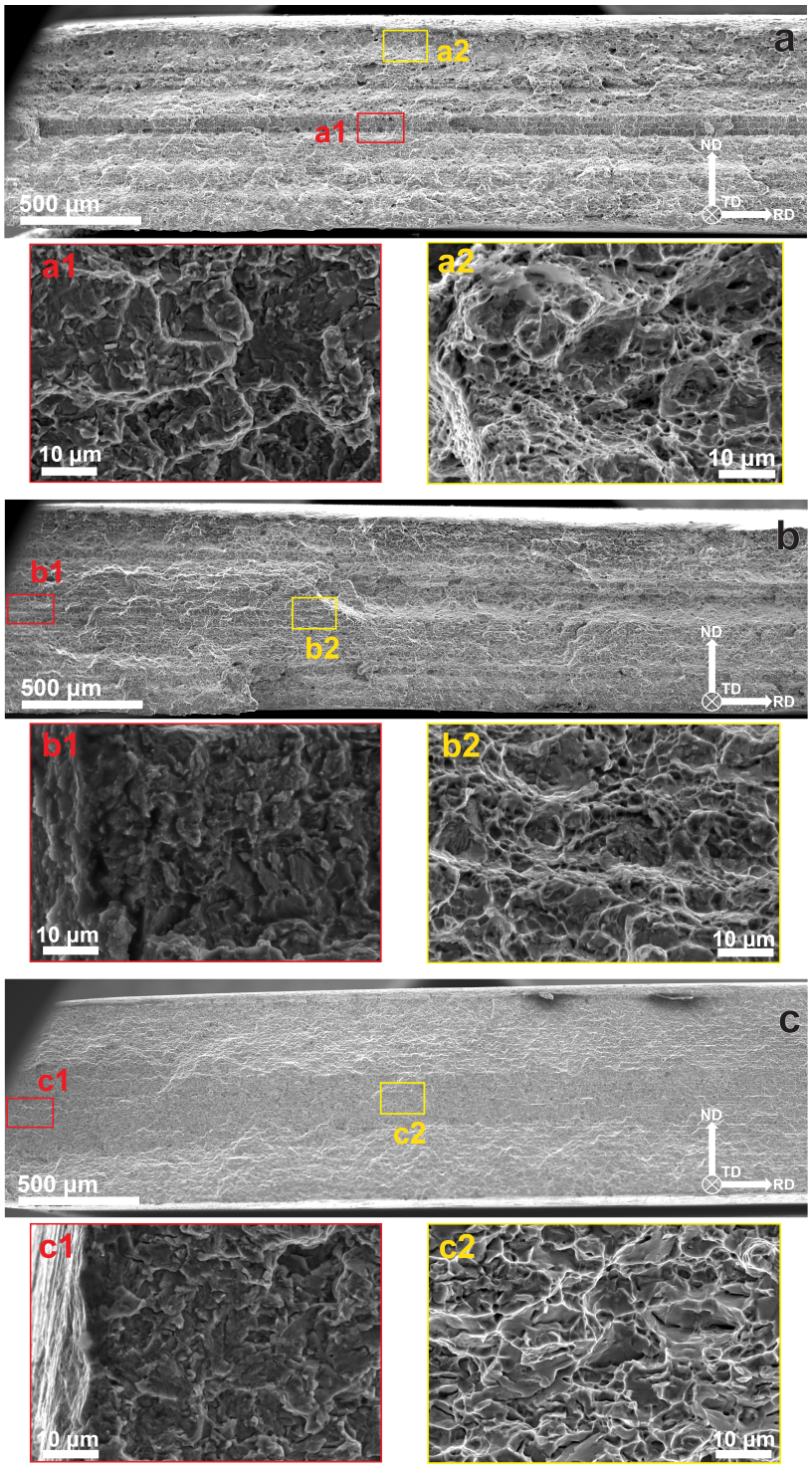

Figure 11. Fracture surface overviews of the (**a**) 590 °C, (**b**) 630 °C and (**c**) 670 °C steels. Insets are shown in red and yellow of brittle and ductile fracture surfaces, respectively.

In order to elucidate why, cross-sectional SEM micrographs are shown in Figure 12. These micrographs show distinct microstructural banding along the rolling direction of the sheet that is still present after the additional heat treatments performed for this work. The 590 °C sample in Figure 12a has a similar banding structure to the 630 °C specimen in Figure 12b, but since the total martensite content is lower, there is a lesser degree of connection between martensite bands in the ferrite matrix. In other words, there are more uninterrupted sections of ferrite between martensite bands compared to the 630 °C specimen which results in an anisotropic martensitic network structure. This promotes fast fracture propagation within the rolling plane rather than through it, leading to banding on the QC fracture surface. The microstructure is most isotropic in the 670 °C specimen in Figure 12c, which translates into more homogeneous crack growth and hydrogen distribution. The effect of a banded microstructure on hydrogen desorption and diffusion has been discussed previously in the literature [37], but it has only sparingly been connected to crack propagation paths [38].

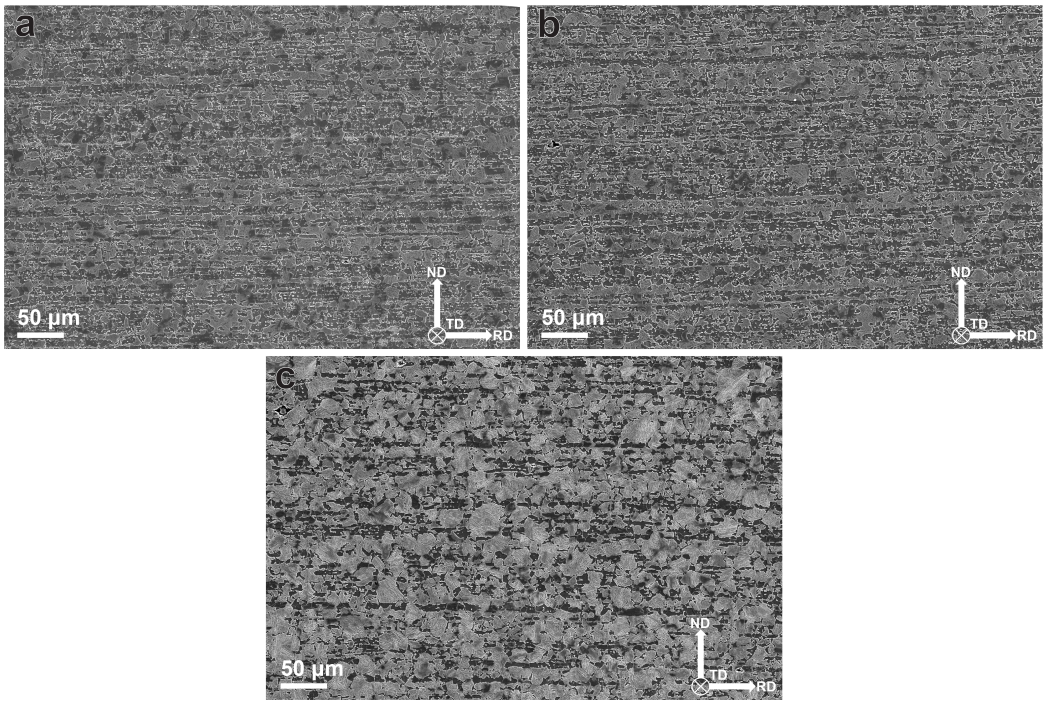

Figure 12. Cross-sectional SEM images of the banded ferrite-martensite structures in the (**a**) 590 °C, (**b**) 630 °C and (**c**) 670 °C specimens.

In summary, the fracture mechanism in these specimens is a combination of early crack initiation and fast crack propagation through martensitic bands. Martensite that is present on the surface gets saturated with hydrogen, which causes brittle QC crack initiation. These cracks propagate easily along connected martensitic grains, which causes a banded structure in the steel with the most microstructural heterogeneity, but this results in the most embrittlement in steels with more homogenous interconnected martensitic networks.

4. Conclusions

This research shows that increasing the martensitic fraction of DP steels leads to a further uptake in hydrogen, but does not increase the extent of HE any further from the moment a connected martensitic network occurs. The increased uptake is a result of the increase in F/M interphase area, which forms the hydrogen trap in the microstructure. The banded anisotropic microstructure is found to cause preferential crack propagation in the rolling direction, which is most pronounced for DP steels containing approximately

50% martensite. Furthermore, it was found that martensite has a large influence on early crack initiation when it is present on the surface that is being charged with hydrogen. The following conclusions can be drawn from the research performed on DP steels:

- The steel annealed at 630 °C shows the most favourable combination of strength and ductility, with a strength of 1025 ± 8 MPa and a fracture strain of 12.6 ± 0.6%. This steel, as well as that annealed at 670 °C, contains connected martensite networks.
- The ferrite/martensite interphase density keeps increasing even after the martensite reaches the required density to form a connected network. This is a result of refinement of ferritic grains resulting in a high aspect ratio and interphase area.
- The steel annealed at 630 °C shows the highest HEI of 86 ± 10%, which is mainly caused by its higher ductility without hydrogen.
- The HEI does not increase further after a martensite content of 50% has been reached, since fracture is dominated by crack propagation through the martensitic phase that is connected in the steels with higher martensite content. This has the added effect that the fracture strain of the specimens annealed at 630 and 670 °C are similar.
- Although the steel annealed at 590 °C shows the lowest HEI at 51 ± 39%, brittle fracture is most evident on the fracture surface of this steel. The localisation of brittle fracture is a result of an anisotropic microstructure in the rolling direction, combined with plasticity effects that increase and localise the hydrogen content.
- Martensite that is present on the surface acts as a brittle fracture initiation point even at high strain rates. Cracks then readily propagate through connected martensite bands. Martensite present on the surface should therefore be avoided to minimise risk of HE in DP steels.

Supplementary Materials: The following supporting information can be downloaded at https://www.mdpi.com/article/10.3390/met15121333/s1, Figure S1: Images used for martensite content and F/M interphase calculations. Figures (a,c,e) were taken from a 590 °C annealed specimen, and (b,d,f) were taken from a 670 °C annealed specimen. (a,b) are taken using SEM, where the martensite is depicted as the cyan phase. (c,d) are OM images, where the ferrite is the phase highlighted in red. (e,f) are EBSD phase maps, where ferrite is depicted in blue and martensite in red.

Author Contributions: Conceptualization, All authors. Investigation, T.B., E.L. and S.F.I. Writing—Original draft, T.B. Writing—Review and Editing, All authors. Supervision; T.B., P.K., A.J.B. and V.P. Funding acquisition, P.K. and V.P. All authors have read and agreed to the published version of the manuscript.

Funding: This research was carried out under project number N19009 in the framework of the Partnership Program of the Materials innovation institute M2i (www.m2i.nl) and the Netherlands Organization for Scientific Research (www.nwo.nl).

Data Availability Statement: The original contributions presented in this study are included in the article/Supplementary Material. Further inquiries can be directed to the corresponding author.

Acknowledgments: The authors extend their gratitude to TATA Steel in IJmuiden for providing the material for this research.

Conflicts of Interest: Author Pascal Kömmelt was employed by the company Tata Steel, Research & Development. The remaining authors declare that the research was conducted in the absence of any commercial or financial relationships that could be construed as a potential conflict of interest.

References

1. Climate TRACE. Distribution of Carbon Dioxide Emissions Produced by the Transportation Sector Worldwide in 2023, by Sub Sector. Available online: https://www.statista.com/statistics/1185535/transport-carbon-dioxide-emissions-breakdown/ (accessed on 22 May 2025).
2. Saidpour, H. Lightweight high performance materials for car body structures. In Proceedings of the NTI Technology Conference, CEME, Ford Motor Company, 16 June 2004. Available online: https://pdfs.semanticscholar.org/8808/d37e012f2b79fcc7db31285e326da1931601.pdf (accessed on 22 May 2025).
3. Galán, J.; Samek, L.; Verleysen, P.; Verbeken, K.; Houbaert, Y. Advanced high strength steels for automotive industry. *Rev. Metal.* **2012**, *48*, 118.
4. Serrenho, A.C.; Norman, J.B.; Allwood, J.M. The impact of reducing car weight on global emissions: The future fleet in Great Britain. *Philos. Trans. R. Soc. A Math. Phys. Eng. Sci.* **2017**, *375*, 20160364.
5. Sezgin, C.T.; Hayat, F. The microstructure and mechanical behavior of TRIP 800 and DP 1000 steels welded by electron beam welding method. *Soldagem Inspeção* **2020**, *25*, e2526.
6. Hilditch, T.; De Souza, T.; Hodgson, P. Properties and automotive applications of advanced high-strength steels (AHSS). In *Welding and Joining of Advanced High Strength Steels (AHSS)*; Woodhead Publishing: Sawston, UK, 2015. pp. 9–28.
7. Zhao, J.; Jiang, Z. Thermomechanical processing of advanced high strength steels. *Prog. Mater. Sci.* **2018**, *94*, 174–242.
8. SSAB. *Dual Phase (DP) Steel: Excellent Ductility and Energy Absorption*; SSAB: Stockholm, Sweden, 2025.
9. Tasan, C.C.; Diehl, M.; Yan, D.; Bechtold, M.; Roters, F.; Schemmann, L.; Zheng, C.; Peranio, N.; Ponge, D.; Koyama, M.; et al. An Overview of Dual-Phase Steels: Advances in Microstructure-Oriented Processing and Micromechanically Guided Design. *Annu. Rev. Mater. Res.* **2015**, *45*, 391–431. https://doi.org/10.1146/annurev-matsci-070214-021103.
10. Rudomilova, D.; Prošek, T.; Salvetr, P.; Knaislová, A.; Novák, P.; Kodým, R.; Schimo-Aichhorn, G.; Muhr, A.; Duchaczek, H.; Luckeneder, G. The effect of microstructure on hydrogen permeability of high strength steels. *Mater. Corros.* **2020**, *71*, 909–917.
11. Mallick, D.; Mary, N.; Raja, V.; Normand, B. Study of diffusible behavior of hydrogen in first generation advanced high strength steels. *Metals* **2021**, *11*, 782.
12. Wang, Z.; Liu, J.; Huang, F.; Bi, Y.J.; Zhang, S.Q. Hydrogen Diffusion and Its Effect on Hydrogen Embrittlement in DP Steels With Different Martensite Content. *Front. Mater.* **2020**, *7*, 620000. https://doi.org/10.3389/fmats.2020.620000.
13. Drexler, A.; Helic, B.; Silvayeh, Z.; Mraczek, K.; Sommitsch, C.; Domitner, J. The role of hydrogen diffusion, trapping and desorption in dual phase steels. *J. Mater. Sci.* **2022**, *57*, 4789–4805. https://doi.org/10.1007/s10853-021-06830-0.
14. Varanasi, R.S.; Koyama, M.; Shibayama, Y.; Chiba, S.; Ajito, S.; Hojo, T.; Akiyama, E. Hydrogen-Induced delayed fracture in a 1.5 GPa dual-phase steel via coalescence of surface and Sub-surface cracks. *Metall. Mater. Trans. A* **2023**, *54*, 2989–2997.
15. Wu, Y.; Qiao, G.; Xu, K.; Xiao, F. Effect of hydrogen on tensile and fatigue properties of ferritic/bainite dual-phase X70 pipeline steel. *Trans. Mater. Heat Treat.* **2023**, *44*, 114–121. https://doi.org/10.13289/j.issn.1009-6264.2023-0072.
16. Liu, M.; Du, C.; Wang, T.; Hai, C.; Li, X. Effect of solution annealing temperature on the hydrogen-assisted cracking behavior of the ferrite-martensite-austenite multiphase stainless steel: The role of ferrite and martensite phases. *Mater. Sci. Eng. A* **2025**, *945*, 148993. https://doi.org/https://doi.org/10.1016/j.msea.2025.148993.
17. Li, Z.; Shi, J.; Fan, Y.; Ma, C.; Dong, X.; Guo, C.; Zhao, H. The effect of intercritical annealing time on the hydrogen embrittlement of dual-phase steel. *Mater. Today Commun.* **2024**, *38*, 108328. https://doi.org/https://doi.org/10.1016/j.mtcomm.2024.108328.
18. Rodoni, E.; Claeys, L.; Depover, T.; Iannuzzi, M. Effect of nickel on the hydrogen diffusion, trapping and embrittlement properties of tempered ferritic-martensitic dual-phase low alloy steels. *Int. J. Hydrogen Energy* **2025**, *98*, 418–428. https://doi.org/https://doi.org/10.1016/j.ijhydene.2024.12.112.
19. Reddy, K.S.; Govindaraj, Y.; Neelakantan, L. Hydrogen diffusion kinetics in dual-phase (DP 980) steel: The role of pre-strain and tensile stress. *Electrochim. Acta* **2023**, *439*, 141727. https://doi.org/https://doi.org/10.1016/j.electacta.2022.141727.
20. Dwivedi, S.K.; Vishwakarma, M. Effect of hydrogen in advanced high strength steel materials. *Int. J. Hydrogen Energy* **2019**, *44*, 28007–28030. https://doi.org/10.1016/j.ijhydene.2019.08.149.
21. Harris, Z.D.; Somerday, B.P. Hydrogen embrittlement of steels: Mechanical properties in gaseous hydrogen. *Int. Mater. Rev.* **2025**, *70*, 394–421. https://doi.org/10.1177/09506608251338698.
22. Davies, R.G. Influence of martensite content on the hydrogen embrittlement of dual-phase steels. *Scr. Metall.* **1983**, *17*, 889–892. https://doi.org/10.1016/0036-9748(83)90255-7.
23. Reddy, K.S.; Govindaraj, Y.; Neelakantan, L. Influence of microstructure on the hydrogen diffusion behavior in dual-phase steels: An electrochemical permeation study. *J. Mater. Sci.* **2022**, *57*, 19592–19611.
24. Drexler, A.; Helic, B.; Silvayeh, Z.; Sommitsch, C.; Mraczek, K.; Domitner, J. Influence of Plastic Deformation on the Hydrogen Embrittlement Susceptibility of Dual Phase Steels. *Key Eng. Mater.* **2022**, *926* , 2077–2091. https://doi.org/10.4028/p-oeev6l.
25. Manda, S.; Kumar, S.; Tripathy, R.R.; Sudhalkar, B.; Pai, N.N.; Basu, S.; Durgaprasad, A.; Vijayshankar, D.; Panwar, A.S.; Samajdar, I. Origin of hydrogen embrittlement in ferrite-martensite dual-phase steel. *Int. J. Hydrogen Energy* **2025**, *100*, 1266–1281. https://doi.org/https://doi.org/10.1016/j.ijhydene.2024.12.411.

26. Takai, K.; Shoda, H.; Suzuki, H.; Nagumo, M. Lattice defects dominating hydrogen-related failure of metals. *Acta Mater.* **2008**, *56*, 5158–5167. https://doi.org/10.1016/j.actamat.2008.06.031.
27. Park, C.; Kang, N.; Liu, S.; Lee, J.; Chun, E.; Yoo, S.J. Effect of Prestrain on Hydrogen Embrittlement Susceptibility of EH 36 Steels Using In Situ Slow-Strain-Rate Testing. *Met. Mater. Int.* **2019**, *25*, 584–593. https://doi.org/10.1007/s12540-018-00221-y.
28. Koyama, M.; Tasan, C.C.; Akiyama, E.; Tsuzaki, K.; Raabe, D. Hydrogen-assisted decohesion and localized plasticity in dual-phase steel. *Acta Mater.* **2014**, *70*, 174–187. https://doi.org/10.1016/j.actamat.2014.01.048.
29. Rodoni, E.; Verbeken, K.; Depover, T.; Iannuzzi, M. Effect of microstructure on the hydrogen embrittlement, diffusion, and uptake of dual-phase low alloy steels with varying ferrite-martensite ratios. *Int. J. Hydrogen Energy* **2024**, *50*, 53–65. https://doi.org/10.1016/j.ijhydene.2023.07.061.
30. Sun, J.; Jiang, T.; Sun, Y.; Wang, Y.; Liu, Y. A lamellar structured ultrafine grain ferrite-martensite dual-phase steel and its resistance to hydrogen embrittlement. *J. Alloys Compd.* **2017**, *698*, 390–399. https://doi.org/10.1016/j.jallcom.2016.12.224.
31. Boot, T.; Kömmelt, P.; Brouwer, H.J.; Böttger, A.; Popovich, V. Effect of titanium and vanadium nano-carbide size on hydrogen embrittlement of ferritic steels. *npj Mater. Degrad.* **2025**, *9*, 2. https://doi.org/10.1038/s41529-024-00546-7.
32. Boot, T.; Kömmelt, P.; Hendrikx, R.W.; Böttger, A.J.; Popovich, V. Effect of plastic deformation on the hydrogen embrittlement of ferritic high strength steel. *npj Mater. Degrad.* **2025**, *9*, 39. https://doi.org/10.1038/s41529-025-00592-9.
33. Fernández Iniesta, S. *Fractographic Study on the Effect of Hydrogen Content in a Dual Phase AHSS on the Mechanism of Hydrogen Embrittlement*; External Research Project Report, TATA Steel in IJmuiden; Delft University of Technology: Delft, The Netherlands, 2023.
34. Drexler, A.; Vandewalle, L.; Depover, T.; Verbeken, K.; Domitner, J. Critical verification of the Kissinger theory to evaluate thermal desorption spectra. *Int. J. Hydrogen Energy* **2021**, *46*, 39590–39606. https://doi.org/10.1016/j.ijhydene.2021.09.171.
35. Martin, M.L.; Fenske, J.A.; Liu, G.S.; Sofronis, P.; Robertson, I.M. On the formation and nature of quasi-cleavage fracture surfaces in hydrogen embrittled steels. *Acta Mater.* **2011**, *59*, 1601–1606. https://doi.org/10.1016/j.actamat.2010.11.024.
36. Merson, E.; Kudrya, A.V.; Trachenko, V.A.; Merson, D.; Danilov, V.; Vinogradov, A. Quantitative characterization of cleavage and hydrogen-assisted quasi-cleavage fracture surfaces with the use of confocal laser scanning microscopy. *Mater. Sci. Eng. A* **2016**, *665*, 35–46. https://doi.org/10.1016/j.msea.2016.04.023.
37. Dunne, D.P.; Hejazi, D.; Saleh, A.A.; Haq, A.J.; Calka, A.; Pereloma, E.V. Investigation of the effect of electrolytic hydrogen charging of X70 steel: I. The effect of microstructure on hydrogen-induced cold cracking and blistering. *Int. J. Hydrogen Energy* **2016**, *41*, 12411–12423.
38. Mohtadi-Bonab, M.; Szpunar, J.; Razavi-Tousi, S. Hydrogen induced cracking susceptibility in different layers of a hot rolled X70 pipeline steel. *Int. J. Hydrogen Energy* **2013**, *38*, 13831–13841.